

Real-Time Investigation of Crystallization and Phase-Segregation Dynamics in P3HT:PCBM Solar Cells During Thermal Annealing

Tiziano Agostinelli,* Samuele Lilliu, John G. Labram, Mariano Campoy-Quiles, Mark Hampton, Ellis Pires, Jonathan Rawle, Oier Bikondoa, Donal D. C. Bradley, Thomas D. Anthopoulos, Jenny Nelson, and J. Emyr Macdonald

Crystallization and phase segregation during thermal annealing lead to the increase of power-conversion efficiency in poly(3-hexylthiophene) (P3HT):[6,6]-phenyl C61-butyric acid methyl ester (PCBM) bulk-heterojunction solar cells. An understanding of the length and time scale on which crystallization and phase segregation occur is important to improve control of the nanomorphology. Crystallization is monitored by means of grazing incidence X-ray diffraction in real time during thermal annealing. Furthermore, the change in film density is monitored by means of ellipsometry and the evolution of carrier mobilities by means of field effect transistors, both during annealing. From the combination of such measurements with those of device performance as a function of annealing time, it is concluded that the evolution of microstructure involves two important time windows: i) A first one of about 5 minutes duration wherein crystallization of the polymer correlates with a major increase of photocurrent; ii) a second window of about 30 minutes during which the aggregation of PCBM continues, accompanied by an increase in the fill factor.

1. Introduction

In bulk-heterojunction (BHJ) solar cells, a nanoscale blend of donor and acceptor materials (such as a conjugated polymer and a fullerene) is used to provide a high interfacial area at which photogenerated excitons can dissociate to yield separate charges.^[1] Efficient conversion of absorbed photons into photocurrent requires sufficiently intimate mixing of the donor and acceptor phases such that photogenerated excitons can easily find an interface, as well as a sufficiently large thermodynamic driving force for charge separation at the interface. At the same time, efficient transport of separated charges towards the electrodes requires a certain degree of phase segregation between the two materials, to enable ordered molecular packing within each phase and also minimize interfacial recombination. The optimum microstructure should thus be a compromise between intimate mixing and complete segregation of the two phases.

The blend of poly(3-hexylthiophene) (P3HT) with [6,6]-phenyl-C61-butyric acid methyl ester (PCBM) is the best-studied material system for organic solar cells and has led to power-conversion efficiencies (PCEs) of ~5%.^[2] Such high efficiency is obtained after a thermal-annealing process which leads to crystallization of the polymer, with consequent higher mobility for holes,^[3] and formation of PCBM aggregates.^[4,5] Other methods have been also proposed to control the morphology of P3HT:PCBM blends, such as slow drying,^[6] vapor annealing,^[7] and additives.^[8] Blend composition is also found to be important,^[9] as is P3HT regioregularity.^[10] In all cases, the phase segregation seems to be driven by the strong tendency of the polymer chains to crystallize, expelling PCBM from the polymer domains. For thermal annealing, device performance, morphology, and crystallization have been monitored as a function of the annealing time by quenching individual samples and comparing the results before and after annealing.^[6,11] However, there have been few studies of changes in i) crystallization,^[12–14] ii) density, and iii) carrier mobilities^[15] in situ during annealing.

Dr. T. Agostinelli, J. G. Labram, Prof. D. D. C. Bradley,
Dr. T. D. Anthopoulos, Prof. J. Nelson
Department of Physics and Centre for Plastic Electronics
Blackett Laboratory
Imperial College London
London SW7 2BW, United Kingdom
E-mail: t.agostinelli@imperial.ac.uk

S. Lilliu, M. Hampton, E. Pires, Dr. J. E. Macdonald
School of Physics and Astronomy
Cardiff University
Queens Buildings
The Parade, Cardiff CF24 3AA, United Kingdom

Dr. M. Campoy-Quiles
Institut de Ciència de Materials de Barcelona
08193 Bellaterra, Catalunya, Spain

Dr. J. Rawle
Diamond Light Source Ltd.
Harwell Science & Innovation Campus
Didcot, Oxfordshire OX11 0DE, United Kingdom

Dr. O. Bikondoa
ESRF, 6 rue Jules Horowitz
BP 220, 38043 Grenoble Cedex 9, France

DOI: 10.1002/adfm.201002076

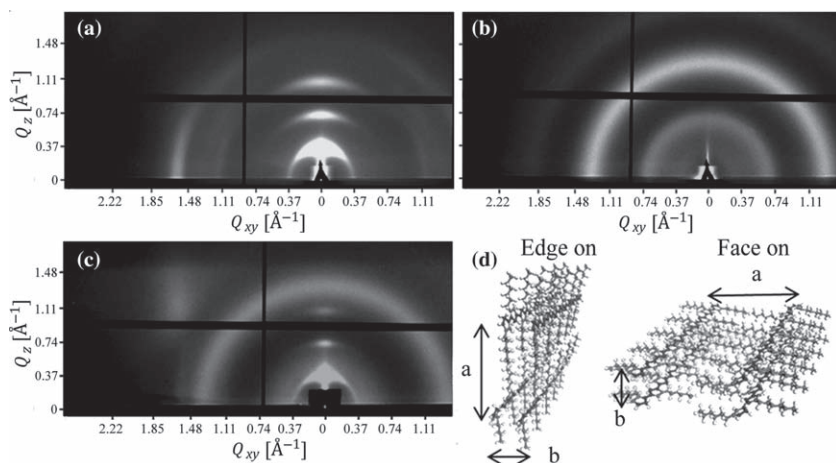


Figure 1. Typical GIXRD patterns for a) P3HT, b) PCBM, and c) P3HT:PCBM (50 wt% PCBM). Also shown is a cartoon of the lamellar stacking structure of P3HT chains in edge-on and face-on orientations.

Here we report on i) detailed grazing-incidence X-ray diffraction (GIXRD) measurements of thin P3HT:PCBM films at different composition ratios during in situ annealing at 140 °C, ii) spectroscopic ellipsometry measurements to monitor changes in film density during annealing, and iii) field-effect hole- and electron-mobility measurements during annealing. Collected data were compared with the performance of photovoltaic devices produced by annealing at 140 °C for different periods of time.

2. Results and Discussion

2.1. Real-Time GIXRD During Annealing

2.1.1. Films

Figure 1 shows typical GIXRD patterns for P3HT, PCBM, and P3HT:PCBM (50 wt% PCBM). Crystalline P3HT self-organizes in lamellar structures with the backbones parallel to the substrate,^[16] the π - π stacking direction of the thiophene rings either perpendicular (face-on configuration) or parallel to the substrate (edge-on configuration), and the alkyl-stacking direction either parallel (face-on configuration) or perpendicular to the substrate (edge-on configuration).^[17] In our samples, all cast from chlorobenzene, P3HT lamellae are mainly edge-on oriented, as shown by the strength of the out-of-plane (OOP) (100), (200), and (300) P3HT peaks and the strong in-plane (010) peak for pure P3HT (**Figure 1**). Lamellar structures are likely to form nanofibrils in our processing conditions^[18] that can be inclined with respect to the substrate, causing the peaks in the diffraction pattern to have an angular spread, as explained by Chabiny et al.^[19]

When P3HT:PCBM solar cells are thermally annealed, they are usually put on a hot plate at a temperature ranging from 75 °C to 155 °C for 4–120 min.^[1] Optimum annealing temperature and time depend on the polymer characteristics, e.g., regioregularity;^[20] also, higher annealing temperatures will require shorter annealing times for the polymer to reach the same final state. After thermal annealing, devices are moved to

a metallic surface at room temperature for fast cooling. For the in situ GIXRD measurements during annealing (presented below) we reproduced this annealing protocol rather than probing the equilibrium structures during gradual heating ramps, to get an insight on the temporal evolution of microstructure that occurs during typical device fabrication protocols. The resulting annealing temperature profile (solid line) is shown in **Figure 2**. The cooling transient is slower than that for heating due to the absence of a cooling stage.

By monitoring the full width at half maximum (FWHM) of the (*h*00) P3HT peaks during annealing, changes in the ordering of P3HT along the alkyl-stacking direction can be tracked. For the crystalline P3HT nanofibrils, the FWHM has contributions from both the size of the crystalline regions, most

closely related to the width of the nanofibrils along the alkyl-stacking direction, and from disorder in the molecular spacings. Separation of these contributions will be the subject of a further paper. Here we discuss the FWHM values for the (100) P3HT peaks, which are least affected by stacking disorder. **Figure 2** shows the reciprocal FWHM of the OOP-(100) P3HT peak during annealing for three different P3HT:PCBM compositions. A strong increase in the reciprocal FWHM, attributed to increased domain size and reduced disorder, occurs in response to the heating step, leveling out after about 5–10 minutes. For higher PCBM content, the response of reciprocal FWHM to heating is relatively slower, which suggests that in as-cast films PCBM molecules are finely mixed with the polymer chains, thus slowing down their crystallization.

In-plane (IP) line profiles are shown in **Figure 3**. While the (100)-P3HT peak is always present in the OOP line profiles, in the IP profiles it assumes a lower intensity, and is clearly visible only in the 33 wt% PCBM sample. This fact means that only a

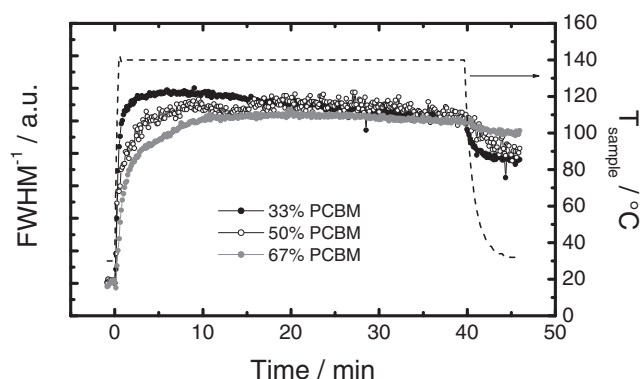


Figure 2. Evolution of reciprocal FWHM with thermal annealing for P3HT:PCBM blend films of different composition. The FWHM is for the OOP-(100) P3HT peak. Curves are normalized to the same heating end point for a direct comparison of transients; absolute values can be found in the Supporting Information. The temperature of the sample during annealing is also shown (dashed line).

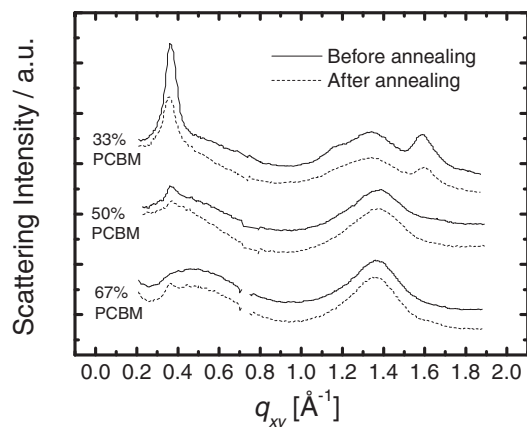


Figure 3. In-plane line profiles of GIXRD images of blend films with increasing PCBM content.

minority of P3HT lamellae are face-on, while most of them are edge-on oriented.

In the 33 wt% and 50 wt% PCBM films the IP (100)-P3HT peak is smaller after annealing, which suggests that the face-on P3HT domains become fewer. However the OOP (100)-P3HT peaks for the same samples sharpen after annealing (Figure 2), which indicates that the edge-on P3HT domains become bigger. Such changes are likely to take place at the expense of the amorphous fraction of P3HT in the blend film. This change differs from the results of Verploegen et al.,^[14] who observed that the face-on orientation is stable to temperatures of ~200 °C. This stability may result from their use of chloroform as a solvent and their thinner (20–25 nm) films as compared with ours (~100 nm). Thinner films are more strongly influenced by the interactions at the substrate-film interface.^[21] In 67 wt% PCBM films the behavior of the face-on phase is different. Though undetectable in as-cast films, upon annealing a weak broad peak at 0.37 Å⁻¹ appears. This result could be due to the PCBM phase weakening the interaction of P3HT with the substrate, thus allowing the growth of crystalline nanofibrils with different orientations at the surface.

The distance between crystallographic planes in the *a* direction (Figure 1) calculated from the OOP-(100) P3HT peaks is shown in Figure 4. The layer spacing increases on heating, largely due to thermal expansion, and decreases again upon cooling but reaches a larger final spacing. This change thus indicates an irreversible structural change as well as linear thermal expansion effects. The thermal expansion coefficient along the OOP-(100) direction calculated in the early stages is $\alpha_T \approx 6.1 \times 10^{-4} \text{ K}^{-1}$. During annealing at a constant temperature of 140 °C the spacing slightly decreases, with respect to the early stages at 140 °C. The final value after cooling is found to be larger for higher PCBM content, possibly due to the presence of PCBM molecules between polymer chains. Our observation extends here to blend films with 67 wt% PCBM content, in contrast with work from Verploegen et al.^[14] who observed the same behavior only up to 50 wt% PCBM content. This difference may relate to the differences in film thickness.

By varying the incident angle α_i with respect to the critical angle α_c we can probe either the surface (top ~10 nm, $\alpha_i < \alpha_c$)

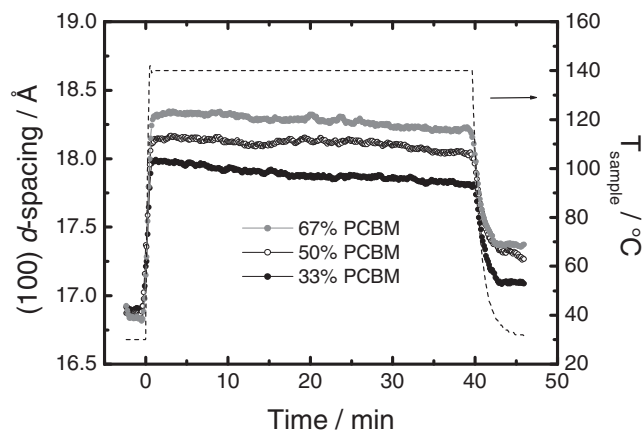


Figure 4. Evolution of (100)-P3HT *d* spacing extracted from OOP line profiles, at different blend concentrations. The temperature of the sample during annealing is also shown (dashed line).

of the film or the bulk of the film for $\alpha_i > \alpha_c$.^[22] If we monitor the ratio *R* of the intensity of the OOP-(100) P3HT peak to that of the main PCBM ring at $q = 1.35 \text{ Å}^{-1}$ versus the incident angle and we assume that peak intensities are proportional to the amounts of crystalline P3HT and PCBM, then we can probe how composition ratio varies at different depths in the film. Consider the quantity $r = R(\alpha_i = 0.25^\circ) / R(\alpha_i = 0.05^\circ)$, i.e., the ratio of *R* above (bulk) and below (surface) the critical angle $\alpha_c = 0.12^\circ$. Changes in *r* before and after annealing reflect vertical segregation of the two components. Table 1 presents the values of *r* before and after annealing for 33 wt%, 50 wt%, and 67 wt% PCBM blend films. It is clear that *r* increases upon annealing, with the relative change being greater for mixtures with higher PCBM content. This observation indicates that PCBM diffuses to the surface, giving a stronger diffraction signal compared to crystalline P3HT. This result is consistent with work from Campoy-Quiles et al.,^[4] where it is reported that upon annealing PCBM molecules diffuse to the surface where they can either aggregate or crystallize.

No crystalline peaks due to PCBM are observed upon annealing, in contrast to the results of Verploegen et al.^[14] who observed cold crystallization at 142 °C. The lack of PCBM crystallization in our case may be due to the greater thickness of our films and the use of a different solvent to cast them, chlorobenzene instead of chloroform. The PCBM ring at $q \approx 1.35 \text{ Å}^{-1}$ observed in the blend is broad and its position and width do not change significantly on annealing. The width of this PCBM ring and the lack of sharp crystalline peaks indicate the presence of small PCBM nanocrystals of ~2-nm dimensions (taking the Debye-Scherrer domain size), consistent with reports in the literature for annealing temperatures close to ours.^[18,23]

Table 1. Vertical segregation parameter *r* before and after annealing for blend films with different compositions (PCBM content is given here).

	33 wt% PCBM	50 wt% PCBM	67 wt% PCBM
<i>r</i> before annealing	1.16	1.11	0.60
<i>r</i> after annealing	1.39 (+19%)	2.06 (+86%)	1.36 (+125%)

In this section we used GIXRD to analyze the evolution of microstructure in typical device-thickness (~ 100 nm) P3HT:PCBM films during in situ annealing and for different blend compositions. We conclude that the ordering of edge-on P3HT crystallites along the alkyl-stacking direction increases upon annealing, whilst the number of face-on P3HT crystallites decreases. P3HT crystallization mainly occurs in the first few minutes. After annealing, the PCBM signal is stronger at the surface, which confirms the presence of PCBM aggregates on the surface. The PCBM phase seems to remain amorphous throughout the annealing process.

2.1.2. Devices

In P3HT:PCBM solar cells the active layer is not spun on a Si substrate, but on a glass/indium tin oxide (ITO)/poly(3,4-ethylenedioxythiophene) poly(styrenesulfonate) (PEDOT:PSS) substrate, followed by metallization with a top electrode. Hence we checked if the above dynamics hold in a devicelike structure by comparing with glass/ITO/PEDOT:PSS/P3HT:PCBM/Al (15-nm thick) structures. The Al layer was sufficiently thin for the diffraction from the active layer not to be obscured, though the presence of glass and ITO leads to increased background scattering (diffuse scattering for glass around $q = 1.5 \text{ \AA}^{-1}$, and sharp rings at higher q values for ITO)^[13] that make detailed analysis more difficult (Figure 5). The OOP-(100) P3HT peak is the only clearly visible peak before annealing, which indicates

that P3HT crystallites are mainly edge-on oriented. Upon annealing, the reciprocal FWHM for this peak evolves as for the films on Si substrates, with a rapid increase in the first few minutes. The dynamics is more rapid than for films on Si substrates, possibly due to the presence of Al on top, which reduces the dispersion of heat into the air and thus provides a more effective annealing of the film. The whole (100) P3HT ring, and in particular the IP-(100) peak, becomes more intense during annealing. This change means that the P3HT domains grow and become more randomly oriented during annealing, with no preference for either edge-on or face-on configuration. It is unclear whether this behavior is caused by the buried substrate interface with PEDOT:PSS or by the presence of metal at the top surface. Given the background scattering and the refractive index mismatch at the surface, it is not possible to draw any direct conclusion on the PCBM phase or the vertical segregation in devicelike structures.

2.2. Real-Time Ellipsometry During Annealing

The observation that most of the crystallization of P3HT occurs in the first five minutes of annealing is consistent with observations made using variable-angle spectroscopic ellipsometry (VASE).

Figure 6a shows the deduced refractive index for 50 wt% PCBM-blend films before and after annealing for 15 minutes at 140°C ; other composition ratios are reported in the Supporting Information. The as-spin-coated samples with higher PCBM content exhibit a less-crystalline polymer phase, seen here as a blue-shifted extinction coefficient and a lower intensity shoulder at 625 nm (the origin of this shoulder is directly related to crystallinity).^[24] This result is in agreement with the GIXRD data, and supports the idea that PCBM molecules disrupt the crystallization of P3HT in the as-spin-coated films. Consequently, annealing has a greater effect on the high-PCBM-content samples; the extinction coefficient spectrum evolves from that typical of low crystallinity films to that typical of high crystallinity ones.

We have previously shown that the change in refractive index at wavelengths well beyond the absorption onset can be correlated to changes in film density.^[25] Using the value of the optical constant n at 850 nm, we estimate an increase in film density upon thermal annealing of around 12% for the samples that contain 50 wt% or more PCBM.

The ellipsometric quantity $\tan \Psi$ measured at $\lambda = 510$ nm is plotted as a function of annealing time for a 50 wt% blend film in (Figure 6b). In accordance with previous studies we interpret $\tan \Psi$ as a measure of the density of the polymer film.^[4,26] Upon heating from room temperature, the value of $\tan \Psi$ first decreases, then at $\sim 80^\circ\text{C}$ it increases rapidly until the target temperature of 140°C is reached and thereafter it increases slowly until heating is turned off. Upon cooling, the value of $\tan \Psi$ increases rapidly again, then levels off. We attribute the initial decrease to thermal expansion, and the subsequent increase to the crystallization of P3HT. The change in the sign of the slope of $\tan \Psi$ versus T should occur when the increase in density due to crystallization overcomes the decrease due to thermal expansion; the temperature at which this happens is likely to be affected by heating rate. The rapid increase in

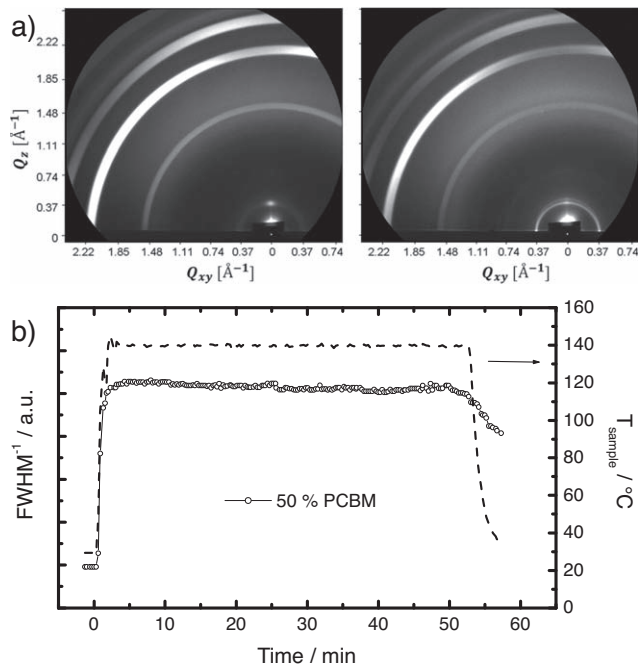


Figure 5. a) GIXRD patterns for as-spun (left) and annealed (right) P3HT:PCBM (50 wt% PCBM) films on a glass/ITO/PEDOT:PSS substrate with a 15-nm-thick layer of Al on top. b) Evolution of reciprocal FWHM with thermal annealing for the same samples. The FWHM is for the OOP-(100) P3HT peaks. Absolute values can be found in the Supporting Information. The temperature of the sample during annealing is also shown (dashed line).

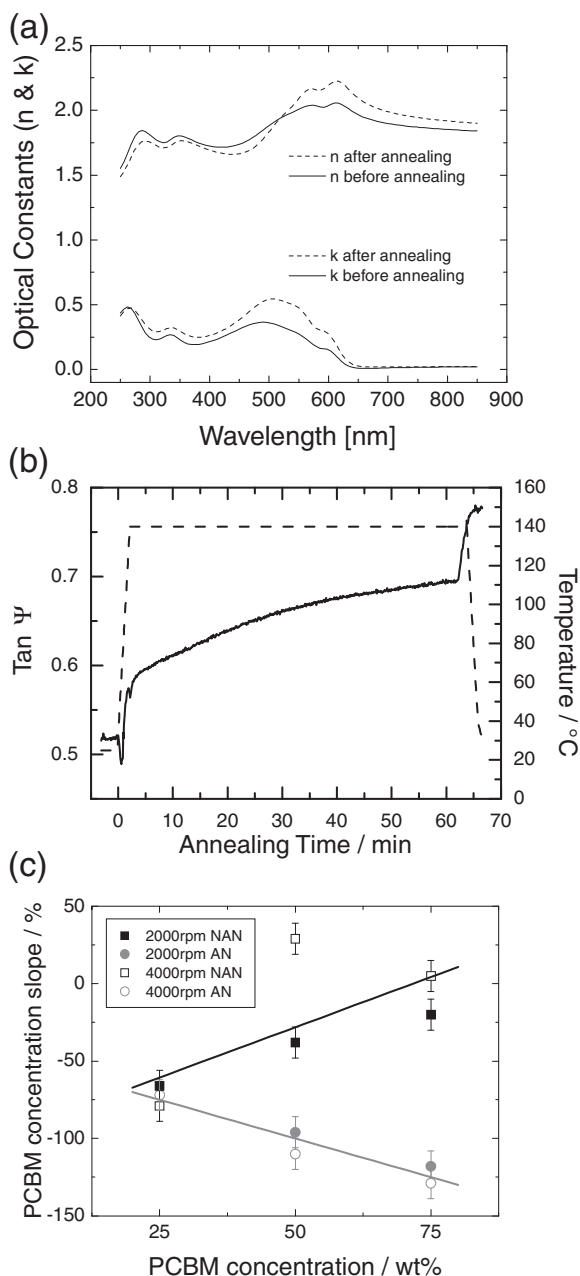


Figure 6. a) Optical constants of a 50 wt% PCBM blend film, before and after 15 minutes annealing at 140 °C. b) Evolution of $\tan \psi$ (solid line), approximately proportional to the polymer density, during thermal annealing for a 50 wt% PCBM blend film; the annealing temperature is also shown (dashed line). c) Slope of the vertical segregation as a function of composition (AN = annealed, NAN = not annealed).

density in the first minutes correlates well with the rapid initial growth in reciprocal FWHM observed using GIXRD (Figure 2). On the other hand, the slower increase occurring throughout the heating process at 140 °C must have a different explanation, as reciprocal FWHM values show a plateau and indeed a gradual decrease on that timescale. The slower increase may be due to the continuous depletion of PCBM molecules towards the surface, which diffuse from the bulk allowing P3HT to

become more densely packed. Upon cooling to room temperature, a contraction occurs equivalent to the initial thermal expansion. As a result, the final film is significantly denser than the as-spin-coated film, in agreement with changes in film density calculated from Figure 6a.

In order to study the effect of composition on phase segregation, following our previous studies^[4] we measured blend films of different composition and modelled the response using a blend layer containing a linear vertical gradient in the concentration of the two components. The linear gradient is characterized by an equation of the type: $c(x) = x \cdot S + c(x = d/2)$, where $c(x)$ corresponds to the concentration of PCBM at a distance x from the substrate, S is the slope of the linear profile, and d is the film thickness. In this respect, $S = 0$ means no vertical segregation, $S < 0$ means a PCBM-rich region close to the interface with the substrate, and the phase segregation increases with an increased absolute value of S . Figure 6c shows the deduced linear slopes as a function of PCBM concentration and annealing. For the as-spin-coated films, increasing PCBM content leads to more homogeneous films (S closer to zero), which is consistent with a more amorphous structure. Thermal annealing, on the other hand, increases the degree of phase separation (the absolute value of S increases), especially for the films with high PCBM content. These results are consistent with the GIXRD data shown in Table 1; vertical segregation becomes more pronounced during annealing with increasing PCBM content.

2.3. Real-Time Hole and Electron FET Mobilities During Annealing

While GIXRD and VASE give mainly access to the surface and bulk properties of the films, organic field-effect transistors (OFET) with bottom gate and bottom source and drain contacts can provide insight into the evolution of morphology at the interface with the substrate (dielectric).^[27] Figure 7 shows how the linear field-effect mobility of electrons and holes in a P3HT:PCBM 50 wt% blend film on a hydrophobic substrate

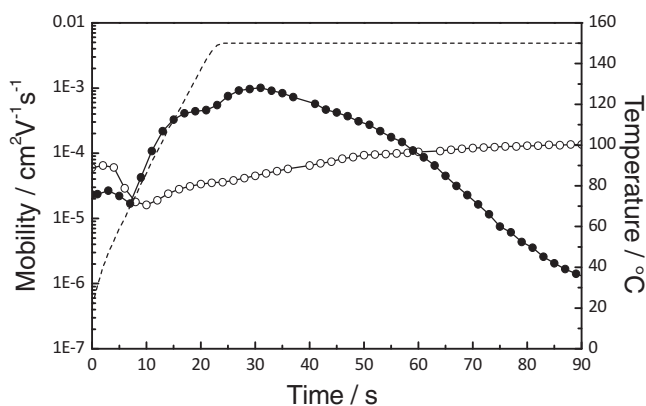


Figure 7. Field-effect hole (open circles) and electron (filled circles) mobilities as a function of time during thermal annealing (dashed line), on HMDS-treated SiO₂. Final mobilities after cooling of holes and electrons are $1.02 \times 10^{-4} \text{ cm}^2 \text{ V}^{-1} \text{ s}^{-1}$ and $8.24 \times 10^{-7} \text{ cm}^2 \text{ V}^{-1} \text{ s}^{-1}$, respectively.

(SiO₂ treated with hexamethyldisilazane (HMDS)) vary with annealing time at 150 °C. To correctly interpret the results, it should be noted that the heating ramp from room temperature to high temperature is not as steep as with the in situ measurements shown above, as it is here limited to 5 °C min⁻¹. Mobility of holes μ_h first becomes smaller as heating starts. Then, when 100 °C is reached, μ_h starts to increase steeply to a plateau around 1×10^{-4} cm² V⁻¹ s⁻¹. Electron mobility μ_e starts to increase soon after heating starts, and reaches a maximum value of 1×10^{-3} cm² V⁻¹ s⁻¹. We attribute this to the increased mobility of polymer chains and to the consequent diffusion of PCBM between them towards the interface with the substrate, in accordance with the work of Campoy-Quiles et al.^[4] This interpretation explains both the drop in hole mobility, due to disruption of the P3HT connected phase, and the simultaneous increase in electron mobility, thanks to a better electron-percolation network close to the interface with the substrate. Conversely, as soon as the temperature is high enough for crystallization of P3HT to take place, hole mobility starts to increase, and correspondingly electron mobility starts to increase at a slower pace and then decreases. While hole mobility improves thanks to a better coupling between polymer chains after crystallization, electron mobility decreases due to the expulsion of fullerenes from the polymer-rich phase, leading to a less-connected PCBM network close to the all-important (for transistors) dielectric interface at the substrate. We further note in that context that crystallization of polymer thin films is believed to proceed from the substrate–film interface through the remainder of the film.^[16] The rate of change of electron mobility is less negative at the lower temperature (not shown). Similar trends are observed in P3HT:PCBM blend transistors that use bare (hydrophilic) SiO₂ dielectrics (shown in the Supporting Information), where, however, μ_e is one order of magnitude lower before annealing and becomes undetectable soon after heating starts; the trap states in bare SiO₂ are known to suppress the electron channel in organic transistors.^[28] The value of μ_h levels off more quickly for bare SiO₂ compared to in SiO₂/HMDS, possibly because of the weaker interaction between polymer chains and the SiO₂, which facilitates microstructural modifications induced by temperature. By comparing the timescales on which hole and electron mobilities change, it can be concluded that the aggregation of PCBM molecules or nanocrystals proceeds on a longer timescale than does P3HT crystallization. This conclusion is consistent with GIXRD and VASE measurements, from which we deduced that the crystallization of P3HT occurs soon after annealing commences and cannot, therefore, explain the residual change in density of the film after the first, short, time window. Given that FETs mainly probe the buried interface, from the observation of timescales on which crystallization occurs, we conclude that P3HT crystallization proceeds more quickly at the surface of the film than close to the interface with the substrate.

2.4. Solar Cells Annealed at Different Times

Finally, we studied the performance of P3HT:PCBM photovoltaic devices as a function of annealing time. Individual devices prepared in the same way were annealed for varying

lengths of time at 140 °C and characterized by measuring the current density J versus voltage V characteristics under solar-simulator (AM1.5-filtered) irradiation. The evolution of the sample temperature was the same as also used for our in situ GIXRD and VASE measurements. However the cooling step was quicker here, as samples were quenched on a room-temperature metallic surface at the end of the annealing; this is not possible with in situ measurements, where the cooling speed reflects that of the heating stage. The results show that, in correspondence to the first crystallization of P3HT, there is a major increase in the short-circuit current (J_{sc}) over the first five minutes, which is reflected in a steep increase of PCE (Figure 8). The PCE then continues to increase more slowly, partly due to a minor increase in J_{sc} and to a continuing increase of fill factor (FF). We attribute the initial increase of PCE to the crystallization of P3HT, as indicated by GIXRD and VASE data, and the subsequent improvement to the continuing aggregation of PCBM during annealing, as indicated by VASE and OFET data. P3HT crystallization improves J_{sc} for two reasons: First, crystallization leads to a better absorption in the near-infrared

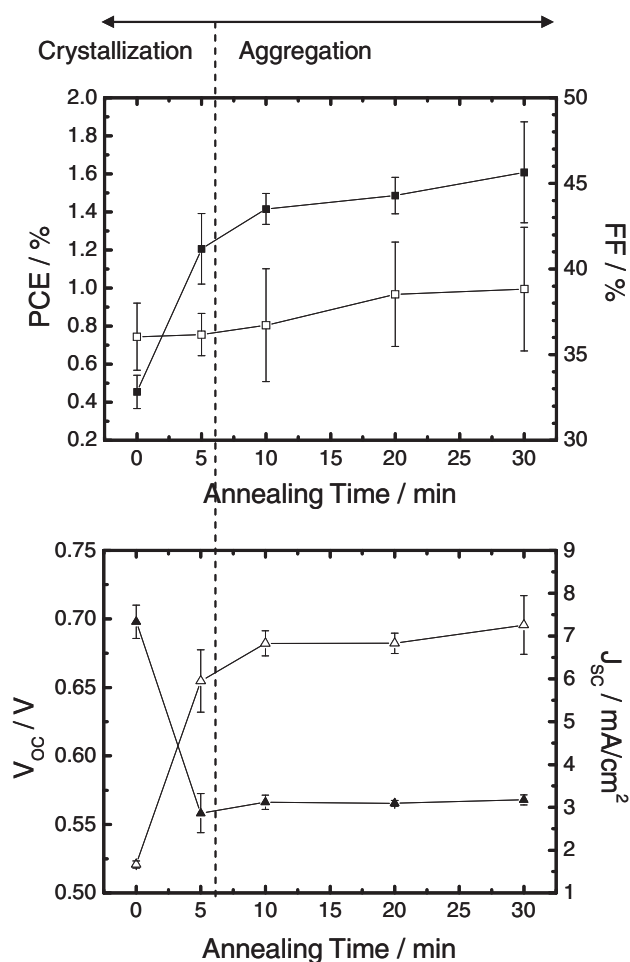


Figure 8. PCE (filled squares), FF (open squares), V_{oc} (filled triangles), and J_{sc} (open triangles) values for P3HT:PCBM (50 wt% PCBM) blend solar cells as a function of annealing time. Each point is an average over more than five devices and the error bars represent the standard deviation.

region of the solar spectrum and second, it yields a higher hole mobility that prevents geminate-pair recombination.^[29] On the other hand, the continuing aggregation of PCBM assists charge collection through the formation of a network for efficient electron transport, thus preventing losses due to bimolecular recombination. It should be noted that in devices the bottom interface of PCBM is with hydrophilic PEDOT:PSS, which is absent from most of the structures studied with GIXRD, VASE, and OFET. This absence is because for these measurements PEDOT:PSS masks the underlying dynamics and makes the interpretation of results more difficult. However, care was taken to use hydrophilic substrates: Si for GIXRD, fused silica for VASE, and SiO₂ (with and without HMDS coating) for OFET measurements. Also, a restraining top electrode is absent from most of the structures studied in the earlier sections. As discussed in Section 2.1.2, the presence of the top electrode is likely to speed up the crystallization of P3HT. In summary, we propose the following evolution of the microstructure during annealing of P3HT:PCBM bulk heterojunction solar cells: Increase of polymer chain mobility initially occurs allowing PCBM to diffuse toward the substrate, followed by crystallization of polymer chains in the first ~5 minutes. This step lasts longer at the buried interface of the P3HT:PCBM film with the substrate due to reduced structural freedom. PCBM molecules aggregate continuously throughout the duration of annealing, which leads to diffusion of PCBM towards the surface.

3. Conclusions

In conclusion, thanks to in situ GIXRD, VASE, and FET mobility measurements, we were able to demonstrate that the initial increase of power conversion efficiency in P3HT:PCBM solar cells during thermal annealing correlates with the crystallization of P3HT in an initial fast time window. Thereafter, PCE continues to increase, but at a much slower pace, probably due to the ongoing diffusion of PCBM. Our work helps to better understand the dynamics of microstructure in P3HT:PCBM solar cells during thermal annealing.

4. Experimental Section

Materials and Solutions: Regioregular P3HT was synthesized by Merck Chemicals and used as received. M_n , M_w , polydispersity index, and regioregularity were 19.5 KD, 34.1 KD, 1.74, and 94.7%, respectively. PCBM (99.5% purity) was used as received from Solenne BV. Blend solutions (P3HT:PCBM = 2:1, 1:1, 1:2, by weight) were prepared using chlorobenzene (30 mg ml⁻¹ for films and 60 mg ml⁻¹ for devices). The solutions were stirred overnight to promote complete dissolution.

GIXRD: 1 mm thick silicon substrates (IDB Technologies) were cleaned in sequence with acetone (15 min) and isopropanol (15 min) using an ultrasonic bath, and then dried using a nitrogen gun. The blend films were then prepared by spin-coating their respective solutions at spinning speeds varying between 1300 and 1800 rpm on top of cleaned substrates, which resulted in thicknesses between 95 and 130 nm. The GIXRD technique has been reviewed previously.^[10,30] GIXRD measurements were performed at the I07 beamline (Diamond Light Source, UK). A chamber provided with a hotplate, on which the samples were glued with conductive silver paint, and a system of motorized shields and slits to reduce the background noise, was mounted on

a 2 + 3 circle diffractometer with a hexapod sample stage. During annealing, the sample temperature was controlled with a Eurotherm 2704 temperature controller by means of a thermocouple thermally connected to the top of the film (sample temperature overshoot ~2.5 °C, settling time ~20 s, accuracy after settling ±0.05 °C). The chamber was filled with helium before the experiments started to avoid air scattering. A monochromatic radiation of 10 KeV energy and resolution of $<1 \times 10^{-4}$ KeV were used. Diffraction patterns were detected with a PILATUS 100K (Dectris) Si photodiode array detector. Single images were collected every 7.45 ± 0.25 s, as a compromise between high signal-to-noise ratio and high sampling rate. After aligning the sample and detecting the critical angle α_c , a standardized set of scans was performed for all the samples. Images were collected before, during (at 140 °C for 40 min), and after annealing. Incident-angle scans, from $\alpha_i = 0.05^\circ$ up to $\alpha_i = 0.25^\circ$ before, and after annealing were also performed. The blend film deposited on ITO/PEDOT:PSS substrates and metalized with Al were measured using the BM28 beamline at ESRF (European Synchrotron Radiation Facility), where experimental details were as above except for the use of a 6-circle diffractometer, and a MAR area detector. A graphical user interface (GUI) for the grazing incidence X-ray diffraction-image analysis, provided with image treatment, center detection, conversion from pixels to q coordinates, batch fitting, region-of-interest analysis, etc., was developed. For each set of experiments, after direct beam-center detection, image pixel coordinates were converted into q values. OOP line profiles with azimuthal angle $\theta = 90^\circ$ and IP line profiles with $\theta = 0^\circ$ were batch-extracted and smoothed. OOP and IP line profiles were fitted using an empirical background function and Pearson VII functions for the peak profiles, from which the d spacings and peak widths were extracted.

VASE: VASE was applied using a SOPRA rotating-polarizer ellipsometer (GES-5) on samples spin-coated at 2000 rpm and 4000 rpm over fused silica substrates. The complex refractive index for samples with different compositions was deduced using the standard critical-point model of the dielectric function.^[25] These data were also analyzed using the Bruggeman effective medium approximation, by mixing the pure P3HT and PCBM optical constants with a model that included vertical segregation.^[4] We compare the optical constants deduced ex situ before and after annealing at 140 °C for 15 minutes in a dry N₂-filled glovebox. In addition, we performed real-time studies during annealing at a single wavelength (510 nm); for this, the samples were kept on a Linkham hot stage with a N₂ flux to prevent degradation. After an initial ramp of 50 °C min⁻¹, the temperature was kept constant at 140 °C and the ellipsometric angles recorded.

FET Mobilities: FET devices were made by spin-coating (1800 rpm, 60 s) a solution of P3HT:PCBM = 1:1 in chlorobenzene (30 mg ml⁻¹) on to a cleaned, cleaved Philips (bottom contact, bottom gate) substrate. A schematic cross-section of the bottom gate structure used in this study is given in the Supporting Information. After drying in N₂ for 4 h the devices were encapsulated with two successive cytop coatings (spin-coated at 1500 rpm for 60 s). For FET measurements the samples were transferred to a vacuum probe station and fixed to a mica slide. n- and p-type transfer curves were measured every 2 min during a heating regime, whereby samples were heated at 5 °C min⁻¹ to a maximum temperature of either 135 °C or 150 °C and held there. The linear field-effect mobility was measured as a function of annealing time using standard semiconductor models^[31] and a Keithley 4200 semiconductor parameter analyzer. The hole and electron mobilities of ambipolar OFETs can be measured independently from one another by selectively injecting holes/electrons with the correct choice of applied voltages.^[32]

Devices: Bulk-heterojunction solar cells with the sandwich structure glass/ITO/PEDOT:PSS (50 nm)/P3HT:PCBM (1:1, ~200 nm)/Ca(20 nm)/Al (120 nm) were fabricated and annealed at 140 °C in a N₂ atmosphere on a hot plate for different times after evaporation of the top contact. All devices were illuminated through the semitransparent ITO electrode with AM 1.5 light from a filtered Xe lamp at an intensity of 100 mW cm⁻². The light J - V characteristics were recorded using a Keithley 237 electrometer.

Supporting Information

Supporting Information is available from the Wiley Online Library or from the author.

Acknowledgements

This work was partially funded by the Engineering and Physical Sciences Research Council (EPSRC) grant numbers EP/F023200 and EP/F016255, Research Councils UK (RCUK). TDA is an RCUK Fellow/Lecturer. DDCB is the Lee-Lucas Professor of Experimental Physics.

Received: October 1, 2010

Revised: November 10, 2010

Published online: March 7, 2011

- [1] G. Dennler, M. C. Scharber, C. J. Brabec, *Adv. Mat.* **2009**, *21*, 1323.
- [2] J. Y. Kim, S. H. Kim, H. H. Lee, K. Lee, W. L. Ma, X. Gong, A. J. Heeger, *Adv. Mat.* **2006**, *18*, 572.
- [3] a) V. D. Mihailetschi, H. X. Xie, B. de Boer, L. J. A. Koster, P. W. M. Blom, *Adv. Funct. Mat.* **2006**, *16*, 699; b) M. Caironi, T. Agostinelli, D. Natali, M. Sampietro, R. Cugola, M. Catellani, S. Luzzati, *J. Appl. Phys.* **2007**, *102*, 024503.
- [4] M. Campoy-Quiles, T. Ferenczi, T. Agostinelli, P. G. Etchegoin, Y. Kim, T. Anthopoulos, P. N. Stavrinou, D. D. C. Bradley, J. Nelson, *Nat. Mat.* **2008**, *7*, 158.
- [5] L. M. Chen, Z. R. Hong, G. Li, Y. Yang, *Adv. Mat.* **2009**, *21*, 1434.
- [6] W. L. Ma, C. Y. Yang, X. Gong, K. Lee, A. J. Heeger, *Adv. Funct. Mat.* **2005**, *15*, 1617.
- [7] G. Li, Y. Yao, H. Yang, V. Shrotriya, G. Yang, Y. Yang, *Adv. Funct. Mat.* **2007**, *17*, 1636.
- [8] a) Y. Yao, J. H. Hou, Z. Xu, G. Li, Y. Yang, *Adv. Funct. Mat.* **2008**, *18*, 1783; b) A. Pivrikas, P. Stadler, H. Neugebauer, N. S. Sariciftci, *Org. Electron.* **2008**, *9*, 775.
- [9] Y. Kim, S. A. Choulis, J. Nelson, D. D. C. Bradley, S. Cook, J. R. Durrant, *J. Mater. Sci.* **2005**, *40*, 1371.
- [10] Y. Kim, S. Cook, S. M. Tuladhar, S. A. Choulis, J. Nelson, J. R. Durrant, D. D. C. Bradley, M. Giles, I. McCulloch, C. S. Ha, M. Ree, *Nat. Mat.* **2006**, *5*, 197.
- [11] a) G. Li, V. Shrotriya, Y. Yao, Y. Yang, *J. Appl. Phys.* **2005**, *98*, 043704; b) K. Inoue, R. Ulbricht, P. C. Madakasira, W. M. Sampson, S. Lee, J. Gutierrez, J. Ferraris, A. A. Zakhidov, *Synth. Met.* **2005**, *154*, 41.
- [12] a) H. J. Kim, H. H. Lee, J. J. Kim, *Macromol. Rap. Comm.* **2009**, *30*, 1269; b) H. J. Kim, J. H. Park, H. H. Lee, D. R. Lee, J. J. Kim, *Org. Electron.* **2009**, *10*, 1505.
- [13] M. Shin, H. Kim, J. Park, S. Nam, K. Heo, M. Ree, C. S. Ha, Y. Kim, *Adv. Funct. Mat.* **2010**, *20*, 748.
- [14] E. Verploegen, R. Mondal, C. J. Bettinger, S. Sok, M. F. Toney, Z. Bao, *Adv. Funct. Mat.* **2010**, *20*, 3519.
- [15] J. G. Labram, E. B. Domingo, N. Stingelin, D. D. C. Bradley, T. D. Anthopoulos, *Adv. Funct. Mat.* **2011**, *21*, 356.
- [16] M. L. Chabinyc, *Polym. Rev.* **2008**, *48*, 463.
- [17] H. Sirringhaus, P. J. Brown, R. H. Friend, M. M. Nielsen, K. Bechgaard, B. M. W. Langeveld-Voss, A. J. H. Spiering, R. A. J. Janssen, E. W. Meijer, P. Herwig, D. M. de Leeuw, *Nature* **1999**, *401*, 685.
- [18] X. Yang, J. Loos, S. C. Veenstra, W. J. H. Verhees, M. M. Wien, J. M. Kroon, M. A. J. Michels, R. A. J. Janssen, *Nano Lett.* **2005**, *5*, 579.
- [19] M. L. Chabinyc, M. F. Toney, R. J. Kline, I. McCulloch, M. Heeney, *J. Am. Chem. Soc.* **2007**, *129*, 3226.
- [20] C. H. Woo, B. C. Thomposon, B. J. Kim, M. F. Toney, J. M. J. Fréchet, *J. Am. Chem. Soc.* **2008**, *130*, 16324.
- [21] D. M. DeLongchamp, B. M. Vogel, Y. Jung, M. C. Gurau, C. A. Richter, O. A. Kirillov, J. Obrzut, D. A. Fischer, S. Sambasivan, L. J. Richter, E. K. Lin, *Chem. Mater.* **2005**, *17*, 5610.
- [22] J. Als-Nielsen, D. McMorrow, *Elements of Modern X-Ray Physics*, John Wiley & Sons Ltd, Chichester, England **2001**.
- [23] Y. Kim, J. Nelson, T. Zhang, S. Cook, J. R. Durrant, H. Kim, J. Park, M. Shin, S. Nam, M. Heeney, I. McCulloch, C.-S. Ha, D. D. C. Bradley, *ACS Nano* **2009**, *3*, 2557.
- [24] U. Zhokhavets, T. Erb, G. Gobsch, M. Al-Ibrahim, O. Ambacher, *Chem. Phys. Lett.* **2006**, *418*, 347.
- [25] M. Campoy-Quiles, G. Heliotis, R. D. Xia, M. Ariu, M. Pintani, P. Etchegoin, D. D. C. Bradley, *Adv. Funct. Mat.* **2005**, *15*, 925.
- [26] M. Campoy-Quiles, P. G. Etchegoin, D. D. C. Bradley, *Synth. Met.* **2005**, *155*, 279.
- [27] G. Horowitz, *J. Mater. Res.* **2004**, *19*, 1946.
- [28] L. L. Chua, J. Zaumseil, J. F. Chang, E. C. W. Ou, P. K. H. Ho, H. Sirringhaus, R. H. Friend, *Nature* **2005**, *434*, 194.
- [29] P. E. Keivanidis, T. M. Clarke, S. Lilliu, T. Agostinelli, J. E. Macdonald, J. R. Durrant, D. D. C. Bradley, J. Nelson, *J. Phys. Chem. Lett.* **2010**, *1*, 734.
- [30] a) M. Birkholz, P. F. Fewster, C. Genzel, *Thin Film Analysis by X-Ray Scattering*, Wiley-VCH Verlag GmbH & Co. KGaA: **2006**; b) G. Renaud, *Surf. Sci. Rep.* **2006**, *32*, 1; c) M. Wolff, A. Magerl, H. Zabel, *Eur. Phys. J. E: Soft Matter Biol. Phys.* **2005**, *16*, 141.
- [31] J. Zaumseil, H. Sirringhaus, *Chem. Rev.* **2007**, *107*, 1296.
- [32] E. C. P. Smits, T. D. Anthopoulos, S. Setayesh, E. van Veenendaal, R. Coehoorn, P. W. M. Blom, B. de Boer, D. M. de Leeuw, *Phys. Rev. B* **2006**, *73*, 205316.